

# CO outflows from young stars in the NGC 2023 cluster

G. Sandell<sup>1</sup>, B. Mookerjea<sup>2</sup>, and R. Güsten<sup>3</sup>

<sup>1</sup> Institute for Astronomy, University of Hawaii at Manoa, 640 N. Aohoku Place, Hilo, HI 96720, USA  
e-mail: gsandell@hawaii.edu

<sup>2</sup> Tata Institute of Fundamental Research, Homi Bhabha Road, Mumbai 400005, India

<sup>3</sup> Max Planck Institut für Radioastronomie, Auf dem Hügel 69, 53121 Bonn, Germany

Last edit March 22, 2024

## ABSTRACT

**Context.** Young early-type HAeBe stars are still embedded in the molecular clouds in which they formed. They illuminate reflection nebulae, which shape the surrounding molecular cloud and may trigger star formation. They are therefore ideal places to search for ongoing star formation activity.

**Aims.** NGC 2023 is illuminated by the Herbig Be star HD 37903. It is the most massive member of a small young cluster with about 30 PMS stars, several of which are Class I objects that still heavily accrete. It might therefore be expected that they might drive molecular outflows. We examined the whole region for outflows.

**Methods.** We analyzed previously published APEX data to search for and characterize the outflows in the NGC 2023 region. This is the first systematic search for molecular outflows in this region. Since the outflows were mapped in several CO transitions, we can determine their properties quite well.

**Results.** We have discovered four molecular outflows in the vicinity of NGC 2023, three of which are associated with Class I objects. MIR-63, a bright mid-infrared and submillimeter Class I source, is a binary with a separation of 2''4 and drives two bipolar outflows orthogonal to each other. The large southeast–northwest outflow excites the Herbig-Haro flow HH 247. MIR-73, a Class I object, which is also a far-infrared source, drives a pole-on outflow. MIR-62 is a Class II object with strong infrared excess and a luminosity of 7 L<sub>⊙</sub>. It is not detected in the far-infrared. The Class I sources have bolometric luminosities of about 20 L<sub>⊙</sub> or lower, that is, they are all low-mass stars. One other far-infrared source, MIR-75, may have powered an outflow in the past because it now illuminates an egg-shaped cavity.

**Conclusions.** The four outflows are all powered by young stars and are located in the immediate vicinity of NGC 2023. They are at a similar evolutionary stage, which suggests that their formation may have been triggered by the expanding C II region.

**Key words.** ISM: jets and outflows – ISM: Herbig-Haro objects – ISM: individual objects: NGC 2023 – stars: pre-main sequence – stars: formation

## 1. Introduction

The reflection nebula NGC 2023 in the L 1630 dark cloud is a well-studied reflection nebula that has been the source of several discoveries. The near-infrared observations by Sellgren (1984) showed that there must be very small dust grains that are transiently heated by a single photon. These are now generally known as polyaromatic hydrocarbons, or PAHs. Fullerenes, the extremely stable C<sub>60</sub> and C<sub>70</sub> molecules, were also found in NGC 2023 (Sellgren et al. 2011). More importantly, however, it has served as a testbed for developing and testing models of photodissociation regions (PDRs) (Black & van Dishoeck 1987; Draine & Bertoldi 1996, 2001; Kaufman, Wolfire & Hollenbach 2006).

NGC 2023 is illuminated by the young B2 Ve star HD 37903. This Herbig Be star is the most massive member of a young stellar cluster with ~ 20 – 30 pre-main-sequence (PMS) stars (Sellgren 1983; DePoy et al. 1990; Mookerjea et al. 2009; López-García et al. 2013). The reflection nebula is embedded in the L 1630 dark cloud at a distance of ~ 400 pc. Most of the PMS stars in the cluster are at the southern and eastern boundary of NGC 2023, where the reflection nebula expands into the dense surrounding molecular cloud, creating a hot PDR (Sandell et al. 2015). Several of the PMS stars are very young Class I sources (Mookerjea et al. 2009) that are heavily accreting and

likely to drive molecular outflows. However, the outflows in the NGC 2023 region have not been studied much so far. Malin, Ogura & Walsh (1987) found a chain of HH objects that is now known as HH 247, in the southwestern boundary of NGC 2023. They were not able to identify the exciting source of the HH objects, although they speculated that MIR-62 would be a likely candidate because of its proximity to the HH objects. Mookerjea et al. (2009) suggested that the HH objects could be excited by the submillimeter/infrared source MIR-63, but stated that this was not a clear identification. We have used the extensive APEX CO data sets from Sandell et al. (2015) to search for and characterize the molecular outflows from young stars in the NGC 2023 cluster. We find four molecular outflows and note that even HD 37903 may drive a weak molecular outflow.

## 2. Observations

### 2.1. APEX and SOFIA observations

All the Atacama Pathfinder EXperiment, APEX<sup>1</sup> (Güsten et al. 2006), and the SOFIA (Stratospheric Observatory for Infrared

<sup>1</sup> APEX, the Atacama Pathfinder Experiment is a collaboration between the Max-Planck-Institut für Radioastronomie, Onsala Space Observatory (OSO), and the European Southern Observatory (ESO).

Astronomy) CO(11–10) and [C II] observations were discussed in detail in Sandell et al. (2015). With APEX, we observed CO(3–2), CO(4–3), CO(6–5), CO(7–6), and  $^{13}\text{CO}(3–2)$ , which are crucial for this paper. We additionally examined the SOFIA observations of [O I] 63  $\mu\text{m}$ , which were presented in Mookerjea et al. (2023). [C II] is generally not an outflow tracer and is not discussed further. Although the [O I] fine structure line at 63  $\mu\text{m}$  can be strongly enhanced in shocks and is often seen in jet-like molecular outflows, it was not detected in any of the outflows either. In Table 1 we list the basic information of the spectral lines that we analyzed for molecular outflow activity. Further details of the observations can be found in Sandell et al. (2015) and Mookerjea et al. (2023). All the spectral lines discussed in this paper were calibrated in main-beam brightness temperature. In order to compare the CO maps more easily, we smoothed the CO(6–5) and CO(7–6) data by regridding them to the same spatial resolution as the CO(4–3) map, that is, 14''4. These smoothed maps are used in all the figures, tables, and analyses presented in this paper.

**Table 1.** Observing setup. The quoted rms sensitivities are in  $T_{mb}$  for a velocity resolution of 0.5  $\text{km s}^{-1}$ .  $\theta_{\text{FWHM}}$  is the half-power beam width, and  $\eta_{\text{mb}}$  is the main-beam coupling efficiency.

Receiver	Molecular transition	Frequency [GHz]	$\theta_{\text{FWHM}}$	$\eta_{\text{mb}}$	rms [K]
FLASH <sup>+</sup>	$^{13}\text{CO}(3–2)$	330.587965	18.5	0.68	0.3
FLASH <sup>+</sup>	CO(3–2)	345.795990	17.7	0.68	0.2
FLASH <sup>+</sup>	CO(4–3)	461.040768	13.3	0.58	0.4
CHAMP <sup>+</sup>	CO(6–5)	691.473076	9.1	0.49	1.3
CHAMP <sup>+</sup>	CO(7–6)	806.651806	7.7	0.48	2.5
GREAT L1	CO(11–10)	1267.014486	23.0	0.67	1.1
upGREAT HFA	[O I] 63 $\mu\text{m}$	4744.777490	6.3	0.63	1.6

## 2.2. UKIDDS images

We retrieved the UKIRT Infrared Deep Sky Surveys (UKIDDS)<sup>2</sup> calibrated images as well as pipeline-reduced photometry of NGC 2023 from the WFCAM science archive<sup>3</sup>. NGC 2023 was observed as part of the Galactic Clusters Survey on 2005 October 14, in all UKIDDS filters. The near-infrared counterpart to MIR-63, a binary with a separation of 2''4, did not have pipeline-reduced photometry. We manually performed photometry using GAIA<sup>4</sup> and APT<sup>5</sup> on both components using 2'' apertures. The photometry for the outflow sources discussed in this paper is given in Table 2.

## 2.3. *Herschel* PACS archive data

NGC 2023 was observed twice with the *Herschel* Space Observatory<sup>6</sup> in the guaranteed time key program, the *Herschel* Gould Belt Survey (HGBS) (André et al. 2010; Bontemps et al. 2010). On operational day (OD) 668 (2011 March 13) NGC 2023 was

<sup>2</sup> The UKIDSS project is defined in Lawrence et al. (2007). UKIDDS uses the UKIRT Wide Field Camera (WFCAM; Casali et al. 2007) and a photometric system described in Hewett et al. (2006).

<sup>3</sup> <http://was.roe.ac.uk>

<sup>4</sup> GAIA is a derivative of the Skycat catalogue and image display tool, developed as part of the VLT project at ESO. Skycat and GAIA are free software under the terms of the GNU copyright.

<sup>5</sup> <http://www.aperturephotometry.org>

<sup>6</sup> *Herschel* was an ESA space observatory with science instruments provided by European-led Principal Investigator consortia and with important participation from NASA.

observed with fast scanning (60''/sec) in parallel mode with PACS (70/160  $\mu\text{m}$ ; AOR 1342215984) and SPIRE. We retrieved the PACS 70  $\mu\text{m}$  level 2.5 JScanam image from the *Herschel* data archive. The field was additionally observed with medium scan speed (20''/sec) and an orthogonal cross scan on OD 513 (2010 October 8) with PACS (100/160  $\mu\text{m}$ ; AORs 1342206080 and 1342206081). These data sets have a much better image quality. Level 2.5 JScanam images were retrieved for both 100  $\mu\text{m}$  and 160  $\mu\text{m}$  from the *Herschel* data archive. All these data sets were discussed in more detail by Stutz et al. (2013). Although PACS photometry of NGC 2023 sources was published by several groups (Furlan et al. 2016; Könuves et al. 2020; Fischer et al. 2020), the deduced flux densities vary strongly, and we found one source, MIR-75, which is visible both at 70  $\mu\text{m}$  and 100  $\mu\text{m}$ , but has no entry in any of the above mentioned papers, nor is it found in the PACS point source catalog at IRSA<sup>7</sup>. We therefore performed photometry using a combination of point-spread function fitting on background-subtracted images using GAIA and MIRIAD (Sault et al. 1995). The PACS photometry is listed in Table 3.

## 3. Molecular outflows

In the radio regime, CO is by far the best tracer of molecular outflows. CO is one of the most abundant molecules after  $\text{H}_2$ , which has no dipole moment and which therefore has no observable transitions at radio wavelengths. CO is easily excited in both diffuse and dense gas. The most accurate mass estimates are obtained by observing at least two rotational transitions and one line of  $^{13}\text{CO}$  (Bachiller & Gómez-González 1992). We have observed five rotational transitions of  $^{12}\text{CO}$  and one  $^{13}\text{CO}$  transition. Molecular outflows can also be studied in a variety of other molecular lines, especially in strong shocks (see e.g. Bachiller & Pérez Gutiérrez 1997), but even in these regions, the CO emission is quite strong. For the purpose of this study, there was no need to observe any other molecular tracer, especially since the non-detection of [O I] 63  $\mu\text{m}$ , a good shock tracer, demonstrates that there are no strong shocks in any of the outflows.

### 3.1. Overview

In order to identify potential outflows more easily, we created channel maps from the CO(3–2) and CO(4–3) images and overlaid the blue- and redshifted channel maps on top of an 8  $\mu\text{m}$  IRAC image in color (see Figure 1). This enabled us to see how the blue- and red-shifted high velocity gas are related to each other and allowed us to identify potential bipolar outflows. In Figure 1, we show blue- and redshifted gas in the velocity range 2 – 8  $\text{km s}^{-1}$  and 13 – 21  $\text{km s}^{-1}$ . We omitted the emission from 8 – 13  $\text{km s}^{-1}$ , which is dominated by cloud emission. These velocity ranges capture almost all of the high-velocity gas. The emission was averaged over 2  $\text{km s}^{-1}$  wide velocity intervals spaced symmetrically around a center velocity of 10.5  $\text{km s}^{-1}$ . We only plot the part of the images with high-velocity gas. After we identified potential outflow sources, we examined the spectra in the vicinity of that source and explored position-velocity diagrams, which is a good way to obtain information about the velocity structure of the outflows.

The dominant outflow source is MIR-63. It is also a submillimeter (MM 3) and a far-infrared source. In the near-infrared, it is a heavily reddened binary. At low redshifted velocities, 13 –

<sup>7</sup> <https://irsa.ipac.caltech.edu>

**Table 2.** Coordinates and UKIDSS magnitudes of the outflow sources in NGC 2023. For saturated sources (marked with <sup>a</sup>), we quote 2MASS magnitudes.

Source	$\alpha_{2000}$ [h m s]	$\delta_{2000}$ [° ' '']	Z [mag]	Y [mag]	J [mag]	H [mag]	K [mag]
MIR-62	5:41:36.390	-2:16:46.1	13.663 ± 0.002	12.818 ± 0.001	11.567 ± 0.001	10.049 ± 0.023 <sup>a</sup>	8.83 ± 0.02 <sup>a</sup>
MIR-63a	5:41:37.178	-2:17:17.3	...	...	...	14.822 ± 0.010	11.24 ± 0.01
MIR-63b	5:41:37.028	-2:17:18.0	...	...	18.70 ± 0.18	14.127 ± 0.006	11.39 ± 0.01
MIR-73	5:41:44.601	-2:16:06.6	19.38 ± 0.13	17.92 ± 0.04	15.832 ± 0.012	12.212 ± 0.001	10.38 ± 0.03 <sup>a</sup>
MIR-75	5:41:44.75	-2:15:54.8	17.39 ± 0.03	15.80 ± 0.01	14.63 ± 0.05	11.44 ± 0.05 <sup>a</sup>	9.99 ± 0.03 <sup>a</sup>

<sup>a</sup> magnitude from 2MASS**Table 3.** Positions and flux densities of Herschel PACS sources in the vicinity of NGC 2023. Positions are derived from the 100  $\mu\text{m}$  image.

Name	$\alpha(2000.0)$ [h m s]	$\delta(2000.0)$ [° ' '']	S(70 $\mu\text{m}$ ) [Jy]	S(100 $\mu\text{m}$ ) [Jy]	S(160 $\mu\text{m}$ ) [Jy]
MIR-63	05:41:37.165	-2:17:16.3	36.5 ± 3.0	35.8 ± 1.0	33.2 ± 3.8
MIR-73	05:41:44.580	-2:16:05.2	13.4 ± 2.0	16.0 ± 0.7	18.2 ± 1.4
MIR-75	05:41:44.760	-2:15:55.3	4.3 ± 0.4	5.4 ± 1.1	...

15 km s<sup>-1</sup>, a wide-angle redshifted outflow lobe is visible, centered on MIR-63 at a PA<sup>8</sup> of  $\sim 130^\circ$ , with a more highly collimated blueshifted (6 – 8 km s<sup>-1</sup>) lobe at a PA of  $\sim -10^\circ$ , which appears to form a misaligned bipolar outflow. Some redshifted emission also surrounds the Class I objects MIR-73 and MIR-75 at  $\sim 120''$  east of HD 37903, where there are no young stars. At these velocities, no gas is observed to be associated with the Herbig Haro flow HH 247<sup>9</sup>, where blueshifted CO emission would be expected.

This picture changes at higher velocities. Faint blueshifted emission centered on the HH 1 cluster is visible there, which was most likely hidden in the relatively strong emission at near cloud velocities from the molecular cloud surrounding NGC 2023. Blue- and redshifted CO emission is also visible toward MIR-73 and MIR-75 at intermediate velocities,  $\pm 5.5$  km s<sup>-1</sup>, but not at higher velocities. A closer examination shows that MIR-73 powers this low-velocity outflow. The blueshifted outflow lobe from MIR-63, which extended all the way to HD 37903 at low velocities, is far more compact at higher velocities and appears to turn by 90° at the position of MIR-62 (see, e.g., CO(4–3) in the velocity range 4 – 6 km s<sup>-1</sup>). At higher velocities, it seems to align with a jet-like feature that is apparently associated with MIR-62, suggesting that it is a separate outflow driven by MIR-62.

At higher velocities, the redshifted outflow from MIR-63 appears to be more collimated, with two prominent peaks east of the star. The northern peak, which dominated at low velocities (13 – 15 km s<sup>-1</sup>), is still strong at 15 – 17 km s<sup>-1</sup>, but we also see a southern peak that completely dominates the emission at higher velocities. A line from the northern peak through MIR-63, that is, at a PA of 84°, that is extended westward passes through HH suggesting that the northern redshifted peak forms a bipolar outflow with HH 1, which is part of the blueshifted counterflow. Likewise, a line from the southern peak through MIR-63, that is, PA = 118°, that is extended westward passes through HH 4. The northern and southern redshifted peaks appear to be part of a single outflow, whose blueshifted counterflow is the Herbig

Haro flow HH 247. This is illustrated in Fig. 1 in the CO(3–2) panel for intermediate velocities, that is, the velocity range 4 – 6 km s<sup>-1</sup> in blue- and 15 – 17 km s<sup>-1</sup> in redshifted CO. We outlined the outflow by the hatched black lines drawn through the two eastern redshifted CO peaks and continuing through MIR-63 to the blueshifted side of the outflow, coinciding with HH 4 and HH 1.

The blueshifted outflow lobe north of MIR-63 must be a separate outflow powered by MIR-63. It would therefore be expected to have a redshifted counterflow to the south, which is indeed the case. At low velocities, a tongue of emission protrudes from MIR-63 at a PA of  $\sim 170^\circ$ , which agrees well with the northern blueshifted outflow, which is at a PA of  $\sim -10^\circ$ . MIR-63 therefore drives two bipolar outflows, a southeast-northwest outflow, and a north-south one. This is expected because we know that it is a binary.

Before we start to derive some basic parameters of these outflows, we review what is known about the outflow sources and what we have learned from the near- and far-infrared photometry presented in this paper.

### 3.2. Outflow sources

#### 3.2.1. MIR-63

MIR-63 is a bright mid-infrared source that Mookerjea et al. (2009) found to coincide with the submillimeter source MM 3. MM 3 was first detected by Wyrowski et al. (2000) at 3 mm with BIMA and also at 850  $\mu\text{m}$  and 450  $\mu\text{m}$  with SCUBA. At the time, there was no known optical or near-infrared counterpart, and therefore Wyrowski et al. assumed that it was most likely a cold starless core. Mookerjea et al. (2009) clearly identified it with MIR-63, however, and they also associated Sellgren’s star D with the same mid-infrared source. They classified MIR-63 as a Class I object and suggested that it might be exciting the Herbig Haro flow HH 247, originally named HH 5, HH 4, and HH 1 by Malin, Ogura & Walsh (1987). We now know that MIR-63 is a heavily reddened binary in the near-infrared (Fig. 2). The eastern component, MIR-63a, is associated with a nebulous arc and is only seen in the H and K bands. This star dominates the emission in the mid- and far-infrared. The western component, MIR-63b, which similarly is heavily reddened, is also detected at J (Table 2). MIR-63b coincides with the optically visible star. It clearly contributes to the emission at mid-infrared wavelengths and appears to have some emission even at 70  $\mu\text{m}$ . In the far-infrared, MIR-63a is quite strong and was detected by PACS in all bands (Table 3).

Although the source appeared to be extended in SCUBA observations, SCUBA did not have the angular resolution to resolve the source. Recently, MIR-63 was observed with ALMA

<sup>8</sup> Position Angle (PA) is measured counterclockwise from north<sup>9</sup> The Herbig Haro flow HH 247 was originally called HH 1, HH 4 and HH 5 by Malin, Ogura & Walsh (1987)

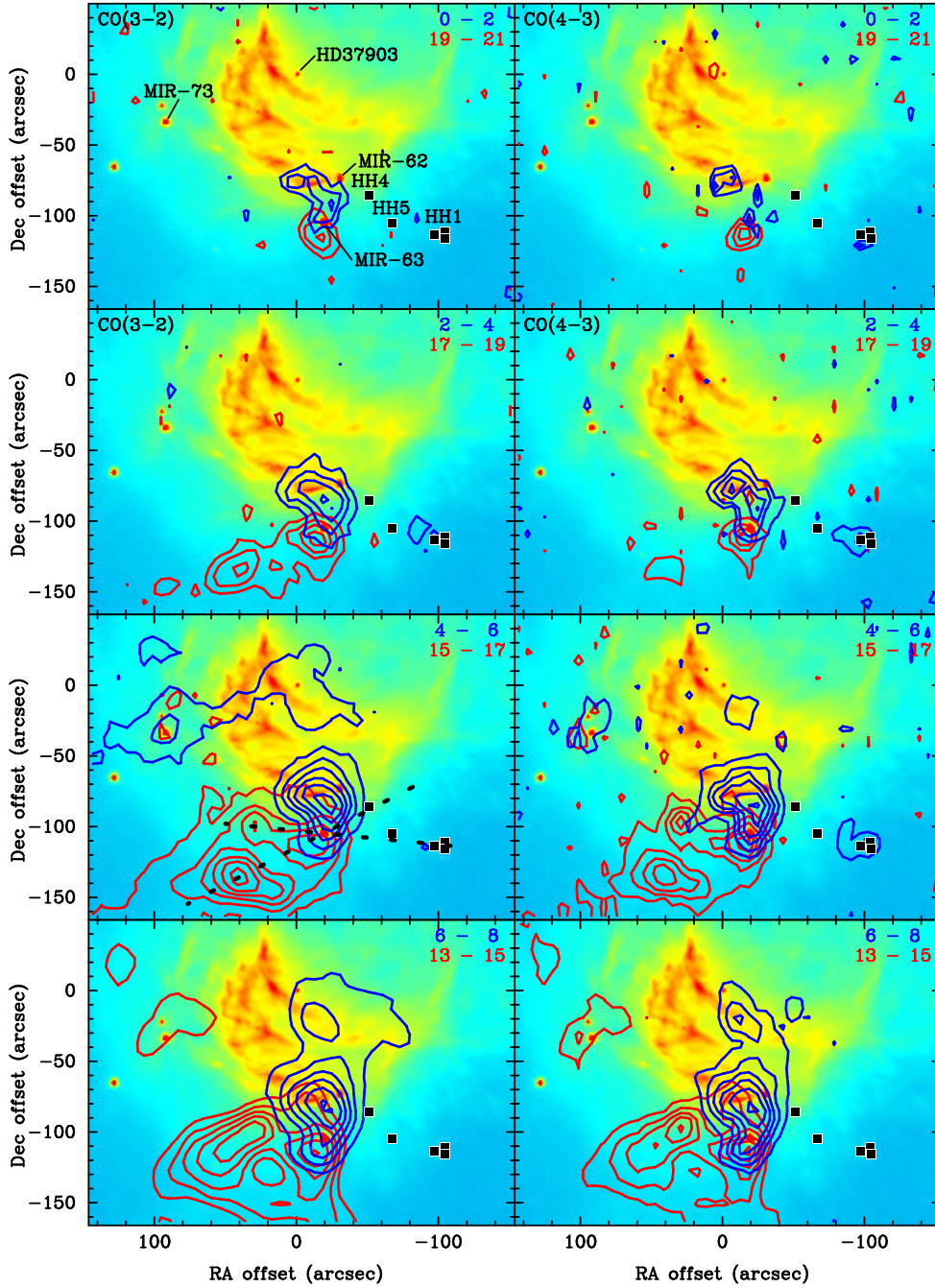


**Fig. 1.** Contours of high-velocity CO emission plotted in  $2 \text{ km s}^{-1}$  wide intervals from a center velocity of  $10.5 \text{ km s}^{-1}$  and overlaid on the  $8 \mu\text{m}$  IRAC image in color. HD 37903 is at an offset  $0'', 0''$ . The left panels show high-velocity emission in CO(3–2), and the right panels show this in CO(4–3). The blue- and redshifted velocity ranges for the CO emission are indicated in the top right corner in each plot. The positions of the young stars MIR-63, MIR-62, and MIR-73 are labeled in the top left panel, and the Herbig Haro objects are plotted with black squares. The hatched lines in the CO(3–2) panel for intermediate velocities are drawn to outline the bipolar outflow from MIR-63. The topmost panels show three linearly spaced contours from  $0.4 \text{ K}$  to  $1.1 \text{ K}$  in CO(3–2), and from  $0.65 \text{ K}$  to  $1.68 \text{ K}$  and  $1.125 \text{ K}$  in red- and blueshifted CO(4–3), respectively. At high velocities,  $\pm 7.5 \text{ km s}^{-1}$ , we plot four contours the from  $0.6 \text{ K}$  for CO(3–2) and  $0.7 \text{ K}$  for CO(4–3), with the highest red and blue contours at  $2.01 \text{ K}$  and  $2.41 \text{ K}$  for CO(3–2) and  $2.12 \text{ K}$  and  $2.46 \text{ K}$  for CO(4–3). For low and intermediate velocities, we plot six contours starting at  $0.8 \text{ K}$  for both CO(3–2) and CO(4–3) at intermediate velocities,  $\pm 5.5 \text{ km s}^{-1}$ , and at low velocities,  $\pm 3.5 \text{ km s}^{-1}$ . The contours start at  $3 \text{ K}$  and  $2.5 \text{ K}$  to avoid contamination from the molecular cloud. For intermediate velocities, the highest contours are at  $6.1 \text{ K}$  and  $6.0 \text{ K}$  and  $4.9 \text{ K}$  and  $6.1 \text{ K}$  for CO(3–2) and CO(4–3), and for low velocities, they are  $11.6 \text{ K}$  and  $16.3 \text{ K}$  and  $12.0 \text{ K}$  and  $15.9 \text{ K}$  for CO(3–2) and CO(4–3), respectively.

and the VLA as part of the VANDAM survey of Orion protostars (Tobin et al. 2020). It was not detected by the VLA, but the continuum emission at  $870 \mu\text{m}$  was resolved by ALMA into two sources, separated by  $2''.4$  (Tobin et al. 2020). The brighter eastern component coincides with our far-infrared source MIR-

63a, while the fainter component coincides with MIR-63b. They marginally resolve MIR-63a as  $0''.19 \times 0''.12$ ; PA =  $3.1^\circ$ , while b is unresolved. MIR-63 was also included in the ALMA Survey of Orion Planck Galactic Cold Clumps (ALMASOP), which observed 72 young dense cores at  $1.3 \text{ mm}$  in three different ar-

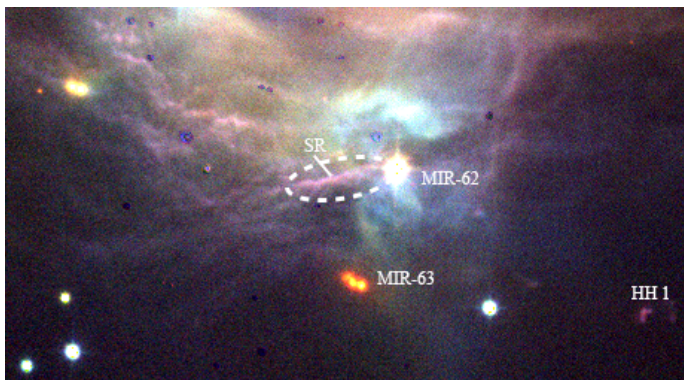


**Fig. 2.** UKIDSS color image (JHK) of the MIR-63 and the MIR-62 region in the southern part of NGC 2023. Both stars are labeled. The very red binary system in the middle of the image is MIR-63. The western component of the binary coincides with the visible star. MIR-62 is  $\sim 65''$  north of MIR-63. We have labeled the bar Sheffer et al. (2011) called SR, the southern ridge, which extends east of the star at a PA  $\sim 110^\circ$ . There is a dark lane (cavity) on the opposite side. We outlined the extent of the blue outflow lobe centered on the southern ridge with a hatched white ellipse. The HH object that Malin, Ogura & Walsh labeled HH 1 is also labeled. In this image, it appears as a faint extended red feature. The size of the image is  $183.6'' \times 101.6''$ .

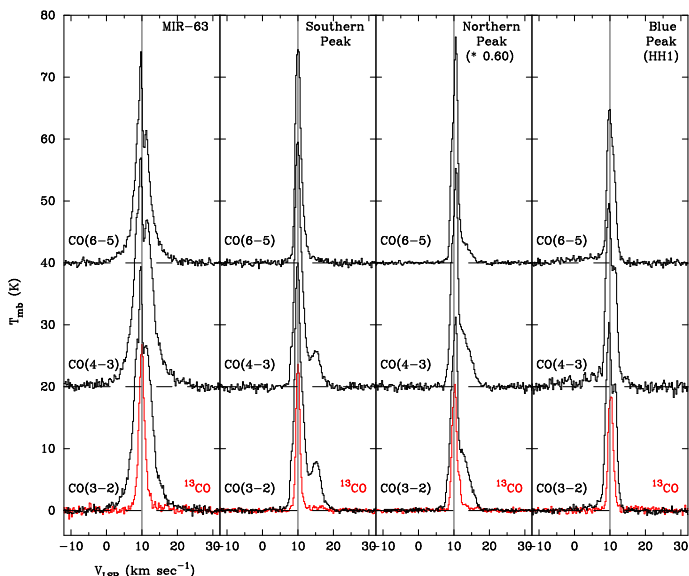


**Fig. 3.** Panel of CO spectra (CO(3–2),  $^{13}\text{CO}$ (3–2), CO(4–3), and CO(6–5)) toward MIR-63, the southern and northern peak in the red outflow, and the blueshifted emission peak near HH 1. MIR-63 is at an offset  $-18''.3, -104''.7$ , the southern peak at  $41''.3, -133''.0$ , the northern peak at  $+30'', -97''$ , and HH 1 at  $-97'', -110''$ . All offsets are relative to HD 37903. The spectra toward the northern peak, where the CO emission is very strong, are scaled by a factor of 0.6. The gray vertical line marks the systemic velocity ( $\sim 10.0 \text{ km s}^{-1}$ ). The spectra for the different CO transitions are offset by 20 K.

ray configurations in continuum and molecular lines (Dutta et al. 2020). They found MIR-63 to be extended and identified four embedded sources in the cloud core. Two of them are compact and coincide with MIR-63a and MIR-63b. These are the same sources that Tobin et al. (2020) detected at  $870 \mu\text{m}$ . The other two were extended,  $\sim 1''$  to  $>3''$ , and appear to be starless cores. They are within 500 au of the two young heavily accreting Class I protostars, both of which drive outflows. Their temperatures are therefore likely to be around 25 to 30 K. A recent paper Luo

et al. (2023) reanalyzed the Dutta et al. ALMA data for MIR-63 and claimed that it drives a complicated molecular outflow that is viewed pole-on. Their analysis of the starless cores showed that they are transient structures for any reasonable assumption of gas temperature. As we already saw in the previous section, MIR-63 drives two molecular outflows, a large southeast-northwest (SE-NW) outflow, and a more compact north-south (N-S) outflow. Neither of them are close to pole-on. The SE-NW component has an inclination of  $\sim 70^\circ$  (see below). The N-S outflow probably has a similar inclination because the red- and blueshifted outflow lobes are spatially well separated.

We derive a bolometric luminosity of  $33.0 \pm 1.2 L_\odot$  using the photometry in Tables 2 & 3 supplemented with Spitzer IRAC and MIPS photometry from Mookerjee et al. (2009). Additionally, we used the tabulated Spitzer IRS photometry points from Furlan et al. (2016). The latter showed that MM 3, or MIR-63a, has a fairly strong silicate absorption feature, indicating that the disk is seen somewhat edge-on. The bolometric temperature is around 200 K for an assumed foreground extinction of 10 mag. Furlan et al. (2016) derived a bolometric luminosity of  $28.2 L_\odot$ . This is slightly lower than what we derive, most likely because of differences in the IRAC/MIPS flux densities. The modeling by Furlan et al. (2016) suggests that the outflow has an inclination of  $70^\circ$ , which sounds very plausible.

In the overview section, we interpreted the outflow emission from MIR-63 seen in Fig. 1 as being composed of two outflows. The large redshifted outflow lobe east of the source is one bipolar outflow, and the blueshifted lobe is faint but still visible in the Herbig-Haro flow HH 247. This outflow is most likely driven by MIR-63a, which was resolved with ALMA by Tobin et al. (2020) to have a roughly north-south oriented disk (PA  $\sim 3^\circ$ ). The second outflow goes roughly north-south, with the blueshifted outflow lobe to the north and the redshifted lobe to the south, partly overlapping with the large eastern redshifted outflow lobe. The position-velocity diagram that goes through the northeastern redshifted peak and the HH objects to the west, that is, PA  $84^\circ$ , (Fig. A.1), shows that to the east, the outflow lobe terminates at  $\sim 80''$  from MIR-63, while the blueshifted outflow lobe extends to  $\sim 100''$ . The position-velocity diagram through the southeastern redshifted peak (Fig. A.2), that is, at a PA of  $118^\circ$ , shows that the redshifted emission is still quite strong at the edge of our CO maps, at  $100''$  from MIR-63, indicating that we do not fully cover the southeastern outflow lobe. In the following, we assume that the redshifted outflow has a total extent of  $110''$ . There is some blueshifted emission to the west, but except for the high-velocity gas associated with HH 1 the blueshifted outflow is largely invisible.

At the position of MIR-63, CO(3–2), CO(4–3), and CO(6–5) show strong blue- and redshifted high-velocity wings extending from about  $-5$  to  $+28 \text{ km s}^{-1}$  (Fig. 3). The systemic velocity, determined from  $^{13}\text{CO}$ (3–2), is  $\sim 10 \text{ km s}^{-1}$ . Only faint high-velocity emission at near cloud velocities is seen in CO(7–6), and CO(11–10) shows no sign of high-velocity emission. The  $^{13}\text{CO}$ (3–2) emission shows clear redshifted high velocity wings not only on MM 3, but also on the northern and southern redshifted peak (Fig. 3), indicating that the redshifted high-velocity gas is somewhat optically thick. At the blueshifted high-velocity peak, which roughly coincides with the HH 1 cluster, the blueshifted emission is stronger in CO(6–5) and CO(4–3) than in CO(3–2), indicating that the blueshifted high-velocity gas in this region is warmer than in the rest of the outflow. Even CO(7–6) shows a blueshifted emission wing extending to a velocity of  $-8 \text{ km s}^{-1}$ . This is the only region where high-velocity emission is seen in CO(7–6).

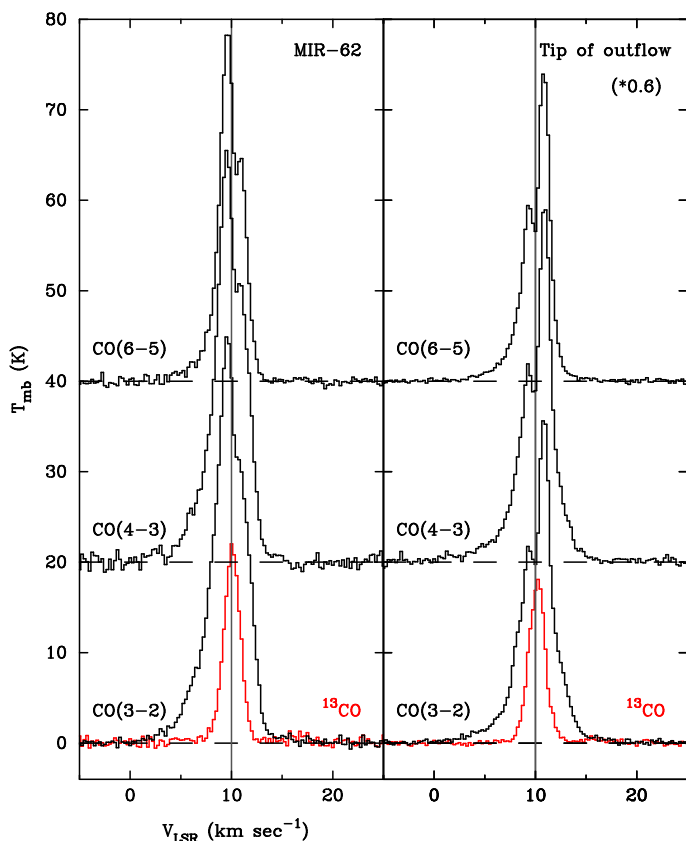


**Fig. 4.** CO spectra toward MIR-62 at an offset  $-30''.0$ ,  $-74''.6$ , and at the tip of the blue outflow lobe at an offset  $+4''.0$ ,  $-81''.1$ . The spectra at the tip of the outflow are scaled by a factor of 0.6, as indicated in the figure. The CO transitions are offset by 20 K for clarity. The  $^{13}\text{CO}(3-2)$  spectra are plotted in red. The vertical gray line marks the systemic velocity ( $\sim 10 \text{ km s}^{-1}$ ) on MIR-62.

The N-S outflow, PA  $\sim -10^\circ$  from MIR-63, is less extended. The blueshifted outflow lobe, which extends to  $\sim 60''$  from MIR-63, shows high-velocity gas to  $\sim -4 \text{ km s}^{-1}$  (total velocity  $14 \text{ km s}^{-1}$ ), while the redshifted gas extends to  $+28 \text{ km s}^{-1}$  (total velocity  $18 \text{ km s}^{-1}$ ; see Fig. A.3). However, since the redshifted outflow lobe overlaps with the redshifted southeastern outflow lobe, some of the emission could also be from the southeastern outflow. There is still high-velocity gas at the edge of our map, indicating that the outflow extends farther than  $45''$  from MIR-63. In our analysis, we assumed that it terminates  $55''$  from MIR-63. As we already mentioned, the N-S outflow is most likely driven by MIR-63b, the optically visible star in the MIR-63 core.

### 3.2.2. MIR-62

MIR-62 (Sellgren’s star C; Haro 5-49) is also a binary with a separation of  $\sim 0''.35$  (Sheffer et al. 2011; Kounkel et al. 2016). It has strong infrared excess and was classified as a Class I/II object by Mookerjea et al. (2009). Megeath et al. (2012) classified it as a Class II source and estimated a foreground extinction of  $\sim 5$  mag. It was not detected by PACS at  $70 \mu\text{m}$ , and it is not a sub-millimeter source. Scarrott, Rolph & Mannion (1989) found that it illuminates a small bipolar reflection nebula oriented north-south (see the JHK image in Fig. 2.) This would suggest that it might drive a north-south outflow, but as we described above, it drives an east-west outflow. However, if the outflow is largely in the plane of the sky, then light would be reflected from the

walls of the east-west outflow. This is most likely the case. Kounkel et al. (2019) found it to have a spectral type of M3. We determine a bolometric luminosity of  $6.7 \pm 0.1 L_\odot$  and a bolometric temperature of  $\sim 1900 \text{ K}$  for an assumed foreground extinction of 5 mag.

Fig. 1 showed that the star appears to power a blueshifted outflow lobe to the east. This outflow lobe is centered on a bright ridge pointing toward MIR-62 (see Fig. 2). Sheffer et al. (2011) argued that this is a PDR feature and named it the southern ridge (SR) because studies of vibrationally excited  $\text{H}_2$  emission (McCartney et al. 1999; Burton et al. 1990) and purely rotational  $\text{H}_2$  lines (Sheffer et al. 2011) showed that these lines are dominated by PDR emission in the southern ridge and are not due to shock excitation. It is a strange coincidence that the southern ridge is so well aligned with the blueshifted outflow lobe if it is not associated with the outflow. The eastern end of the ridge is  $35''$  from MIR-62, while we estimate the length of the outflow to be  $\sim 45''$  ( $0.087 \text{ pc}$ ) from the position-velocity diagram in Fig. A.4.

The outflow velocities are rather modest. At the tip of the outflow, they extend from  $\sim -2$  to  $+16 \text{ km s}^{-1}$  (Fig. 4). There is some redshifted emission at the position of MIR-62, but there is no sign of a redshifted counterflow (Fig. A.4). The UKIDSS JHK color image in Fig. 2 shows a narrow dark structure west of the star, which is approximately aligned with the blueshifted outflow lobe, and which opens up to a faintly limb-brightened cavity farther northwest (like a wine glass). This is most likely created by the counterflow from MIR-62. It is seen even more clearly in the JHK image of Sheffer et al. (2011), their Fig. 1.

### 3.2.3. MIR-73

MIR-73, on the eastern side of the reflection nebula (Fig. 5), was classified as a Class I object by Mookerjea et al. (2009). It has strong near-infrared excess and is relatively bright in the far-infrared. It was easily detected by PACS at all bands (Table 3). It was not detected at  $850 \mu\text{m}$  by SCUBA (Johnstone, Matthews & Mitchell 2006), but Furlan et al. (2016) reported a marginal detection at  $350 \mu\text{m}$ . Furlan et al. (2016) derived a bolometric luminosity of  $17.8 L_\odot$ , and a bolometric temperature of  $277 \text{ K}$  for an assumed foreground extinction of 16 mag. This agrees reasonably well with what we derive, a bolometric luminosity of  $20.9 \pm 0.1 L_\odot$  and a bolometric temperature of about  $260 \text{ K}$  for a foreground extinction of 10 mag.

The systemic velocity of the molecular gas surrounding MIR-73 is  $\sim 10.4 \text{ km s}^{-1}$  (see Fig. 6). The blue- and redshifted emission lobes partly overlap. The separation between the red- and blueshifted peak is  $10''.1$ , suggesting that the outflow is seen almost pole-on (see Fig. 7). The outflow models by Cabrit & Bertout (1986) make an inclination angle of  $20^\circ$  appear about right. The blueshifted peak is almost centered on the star, offset by only  $1''.2$  to the west, while the redshifted outflow lobe is off by  $8''.9$  to the east. We therefore assign an inclination of  $2.4^\circ$  to the blueshifted outflow and leave  $17.6^\circ$  for the redshifted outflow. The outflow velocities are very modest,  $\sim 5 - 6 \text{ km s}^{-1}$  for both outflow lobes (see Fig. 6).

### 3.2.4. MIR-75

MIR-75 was classified as a Class I object by Mookerjea et al. (2009). We see no high-velocity CO toward the star, but it sits at the apex of a limb-brightened cavity on the western side of the star (see Fig. 5). This egg-shaped cavity is seen in all UKIDSS bands, suggesting that it is illuminated by reflected light from

**Table 4.** Physical parameters of the outflows. Dynamical timescales and mass-loss rates are computed using mass weighted velocities. All derived parameters are corrected for inclination. The formulae for the inclination correction factors are given in Bachiller et al. (1990).

Parameter	MIR-63a		MIR-63b		MIR-62	MIR-73	
	red	blue	red	blue	blue	red	blue
Maximum outflow velocity (km s <sup>-1</sup> )	18	15	18	14	12	5.6	5.4
Inclination (°)	70 <sup>a</sup>	70 <sup>a</sup>	70	70	70	17.6	2.4
Temperature (K)	30	75	30	30	40	30	40
Dynamical time scale (10 <sup>3</sup> yr)	5.6	n.a.	3.1	4.3	3.2	14.4	12.3
Mass (10 <sup>-3</sup> M <sub>⊙</sub> )	130	2.4 <sup>b</sup>	52	48	45	2.4	1.5
Momentum (10 <sup>-2</sup> M <sub>⊙</sub> km s <sup>-1</sup> )	160	n.a.	63	47	44	0.99	0.67
Force (10 <sup>-5</sup> M <sub>⊙</sub> km s <sup>-1</sup> yr <sup>-1</sup> )	10.0	n.a.	7.4	3.8	4.8	0.055	0.073
Energy (10 <sup>36</sup> J)	50.4	n.a.	8.6	5.0	1.7	0.014	0.031
Mass loss rate (10 <sup>-6</sup> M <sub>⊙</sub> yr <sup>-1</sup> )	23	n.a.	17	11	14	0.17	0.12

<sup>a</sup> Outflow inclination from Furlan et al. (2016); <sup>b</sup> Mass of HH 1 condensation only

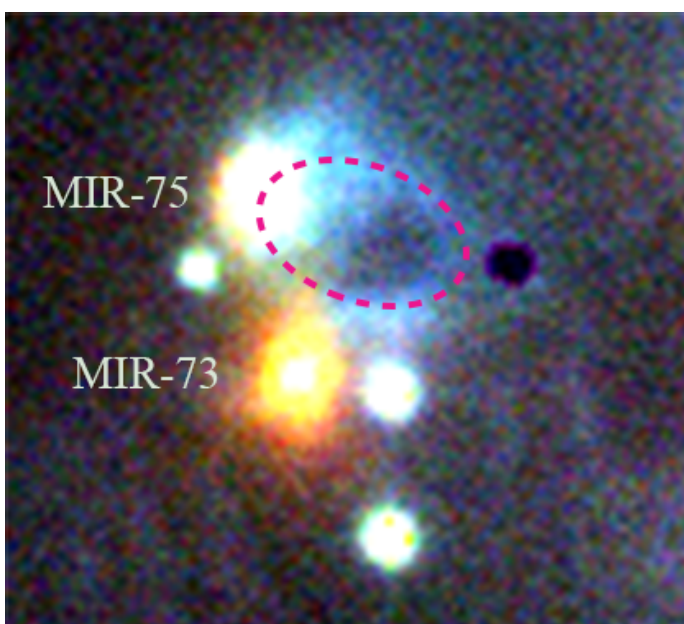


**Fig. 5.** UKIDSS color image (JHK) of the MIR-73 and MIR-75 region east of HD 37903. Both are Class I sources with strong infrared excess, and both were detected by PACS. The stars are labeled. MIR-73, the very red source in the middle of the image, drives a compact almost pole-on outflow. MIR-75 does not appear to drive a molecular outflow, but sits at the apex of a bubble of emission, which we outlined with a dashed red ellipse. The hole west of it is an image artifact. The size of the image is 41''6 × 37''6.

MIR-75. It appears likely that a past outflow may have created the cavity, although there is currently no evidence for outflow activity. MIR-75 is also detected with PACS at 70 and 100 μm and is most likely present at 160 μm as well, but the emission from the star cannot be separated from the strong emission from the surrounding cloud. We derive a bolometric luminosity of  $3.6 \pm 0.2 L_{\odot}$  and a bolometric temperature of  $825 \pm 9$  K, assuming that the foreground extinction is 10 mag, which is similar to the foreground extinction toward MIR-73.

There is no sign of a cavity on the eastern side, possibly because it is obscured by the IR dark cloud filament just east of the star. Another possibility is that MIR-75 is near the edge of the

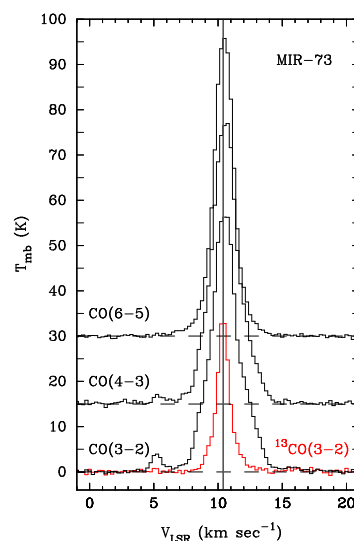


**Fig. 6.** CO spectra toward MIR-73. The left panel shows CO(3–2), and the right panel shows CO(4–3). The <sup>13</sup>CO(3–2) spectrum is also plotted in red in the left panel. The vertical gray line marks the systemic velocity,  $\sim 10.4$  km s<sup>-1</sup>. The narrow emission feature at 5.2 km s<sup>-1</sup> is due to an IR dark cloud filament and not related to the outflow from MIR-73.

NGC 2023 cloud, so that the outflow expanded more freely into the low-density cloud envelope.

### 3.2.5. HD 37903

Wyrowski et al. (2000) found a weak extended ( $\sim 40''$ ) continuum source at 8 GHz centered at  $\sim -10''$ ,  $-12''$  relative to HD 37903. They interpreted this continuum emission as free-free emission from a density enhancement ionized by the Lyman continuum flux from HD 37903. However, PDR tracers such as [C II] and [O I] do not show any enhancement from this continuum source (Sandell et al. 2015; Mookerjea et al. 2023). As we showed in Fig. 1, a blueshifted emission feature lies southwest of the star extending to  $\sim 4$  km s<sup>-1</sup>, that is,  $\sim 6.5$  km s<sup>-1</sup> from the systemic velocity. This blueshifted emission peaks roughly at  $-16''$ ,  $-24''$  from HD 37903 and has a size of  $\sim 50''$ . It is in the same direction as the low brightness continuum emission, suggesting that they may be related. Since we see it in CO(3–

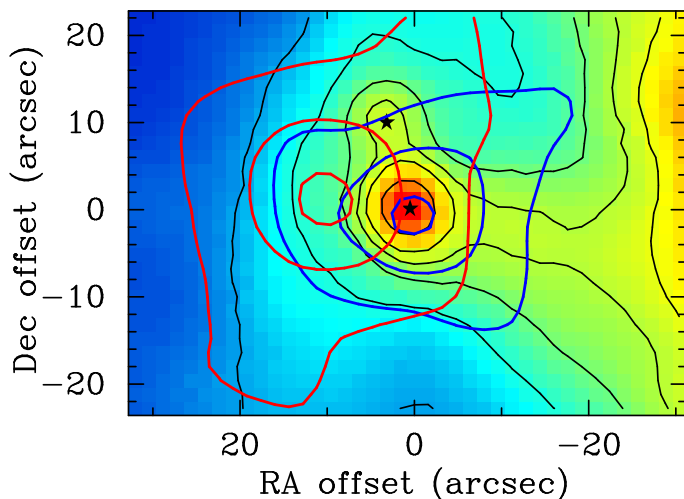


**Fig. 7.** High-velocity emission of CO(6–5) overlaid on a  $100\ \mu\text{m}$  PACS image in color. The blueshifted CO is integrated from  $+6$  to  $+8\ \text{km s}^{-1}$ , and the redshifted CO is integrated from  $13$ – $15\ \text{km s}^{-1}$ . This CO(6–5) map was created with the same angular resolution as CO(4–3) or  $14''.4$ . MIR-73 is placed at an offset  $0'', 0''$ , and MIR-75 is  $\sim 12''$  north of it. Both are marked by black stars.

2), CO(4–3) and CO(6–5), we can estimate the temperature assuming LTE and optically thin emission (see Section 3.3). This gives us an excitation temperature of  $\sim 30\ \text{K}$ . If the blueshifted CO emission were associated with the ionized emission feature, the gas would be expected to be warmer. The cause for this blueshifted CO emission is unclear. Maybe it is just being pushed by the stellar wind from HD 37903. The total mass of the mass of the blueshifted gas  $\sim 0.008\ M_{\odot}$ , which is on the same order as mass in the MIR-73 outflow (see Table 4).

### 3.3. Properties of the outflows

Since we detect all outflows in CO(3–2), CO(4–3), and CO(6–5) and in most cases do not see any high-velocity gas in CO(7–6), we know that the outflowing gas must be warmer than  $20\ \text{K}$ , but probably not much warmer than  $40\ \text{K}$ . There is one exception, however. The blueshifted high-velocity gas associated with the HH 1 cluster is detected even in CO(7–6), and here, we derive a temperature of  $\sim 75\ \text{K}$ . The redshifted counterflow is much colder. To estimate the column densities, we integrated over the outflows in  $2\ \text{km s}^{-1}$  wide velocity intervals from  $-1$  to  $22\ \text{km s}^{-1}$ , except for the velocity range  $8$ – $13\ \text{km s}^{-1}$ , which is dominated by strong molecular cloud emission. For regions in which the outflows overlap, we assumed equal contribution from each outflow. We repeated this for  $^{13}\text{CO}(3-2)$ , although we only detected  $^{13}\text{CO}(3-2)$  line wings in the near cloud velocity ranges, that is, from  $6$ – $8\ \text{km s}^{-1}$  in blueshifted emission and  $13$ – $15\ \text{km s}^{-1}$  in redshifted emission. We can now solve for the optical depth from the ratio of CO/ $^{13}\text{CO}$  by assuming that both have the same excitation temperature and that we know the isotope ratio  $[C/^{13}C]$ , which we assume is  $70$  (see, e.g., Sandell et al. (2015)). In this way, we find that all outflows except MIR-73 are somewhat optically thick at low velocities, with optical depths in the range  $2.5$ – $6$  and a median of around  $3.5$ . For higher velocities, our upper limits suggest that the emission is largely optically thin. We can now determine the excitation temperatures and CO column densities by assuming that CO is in LTE. We can now use the formulae for calculating column densities given by Mangum & Shirley (2015) for optically thin emission and assuming the

excitation temperature is the same for all velocities over each outflow lobe. To do this, we calculated the column density for a grid of temperatures from  $25$ – $50\ \text{K}$  for each CO transition, and then we determined the resulting temperature within the errors with the same column density for each CO transition. For the initial analysis, we gave the near cloud velocities lower weight because we know that they are optically thick. After we constrained an excitation temperature (Table 4), we calculated optical depth corrections for CO(4–3) and CO(6–5) to obtain optical depth-corrected column densities. For each velocity bin, we took the average of the total column densities derived for each transition. The masses given in Table 4 assume that the CO/ $\text{H}_2$  ratio is  $10^{-4}$  and that the total atomic weight per hydrogen atom is  $1.4$  (Kauffmann et al. 2008).

We calculated the outflow parameters largely following the procedures outlined by Lada (1985), Bachiller et al. (1990), and Choi, Evans & Jaffe (1993). To derive the mass, momentum, and energy, we integrated over the same velocity intervals as we use in Fig. 1. All outflow parameters were corrected for inclination using the formulas given in Bachiller et al. (1990) (see also Cabrit & Bertout (1992)). To determine the dynamical timescales, we used the mass-weighted outflow velocity rather than the maximum velocity. The difference compared to using the maximum outflow velocity for our outflow sources is smaller than  $50\%$ . The outflow parameters are given in Table 4.

In the review by Bachiller & Gómez-González (1992), they found that a comparison of different methods for determining the accuracy of the outflow parameters by Cabrit and her collaborators (Cabrit & Bertout 1986; Cabrit, Goldsmith & Snell 1988; Cabrit & Bertout 1992) indicated that the most accurate methods estimate the mass within a factor of 2, the momentum within a factor of 10, and the force within a factor of 20. Even with the extensive CO data set we have, we do not appear to do much better. Our mass estimates are uncertain because of the overlap of outflows and because we average the emission over the whole outflow lobe. This results in large uncertainties in the optical depth correction for gas at low velocities. Furthermore, we are somewhat overcautious in setting the boundary between outflow emission and the ambient cloud, which may contain the bulk of the outflowing gas, resulting in a uncertainty of about a factor of 3. For other outflow parameters, the uncertainty in inclination is the dominant error source. We assumed an inclination angle of  $70^\circ$  for the two MIR-63 outflows as well as for MIR-62. However, the inclination angle for these sources could be as high as  $80^\circ$  or as low as  $50^\circ$ , resulting in uncertainty factors of 4 for momentum, 14 for energy, and 18 for the outflow force, just from the uncertainty in inclination. For MIR-73, the almost pole-on outflow, the errors in momentum and energy due to inclination are small, while the dynamical timescale and force is uncertain by a factor of 10 or more.

## 4. Discussion

All the molecular outflows discovered in the NGC 2023 region are in the immediate periphery of the C II region powered by HD 37903. Furthermore, they all lie in the eastern and southern part of nebula, where the C II region expands into the dense surrounding molecular cloud. This suggests that their formation may have been triggered by the C II region. Elmegreen & Lada (1977) introduced the concept of triggered star formation when they investigated the formation of OB associations, which appear to follow a sequential star-forming mechanism. In this scenario, an H II region ionizes the surrounding molecular gas and drives a shock front into the cloud, accumulating a dense layer of gas

between the ionized gas and the shock front. This compressed gas layer eventually becomes unstable and forms a new OB subgroup. Depending on the density structure of the surrounding cloud, the compressed gas layer may trigger star formation in several different ways, ranging from radiation-driven implosion of pre-existing clouds to a collect-and-compress scenario of the gas layer (see, e.g., Deharveng et al. (2010)). The latter mechanism would also work for a C II region, but instead of triggering OB stars, it would trigger low-mass stars. A good example of collect-and-collapse triggered star formation is the bright H II region RWC 79, which shows a dust emission ring surrounding the ionized gas, in which Zavagno et al. (2006) found two massive fragments that were diametrically opposite to each other, each containing bright near-infrared sources. They identified 12 luminous Class I sources toward the most massive of these dust fragments. It is often difficult, however, to judge whether the expanding H II region has triggered new star formation or just revealed pre-existing dense cores in the surrounding cloud. NGC 2023, however, looks very similar to RWC 79 in the sense that all the young Class I sources are near the periphery of the C II region. Therefore, their formation may well have been triggered by the expanding C II region.

It is clear that when we study the properties of outflows from young stars, both high spatial resolution and sensitivity are required to see large-scale structures and small details. With our moderate spatial resolution,  $\sim 15''$ , we can characterize all the outflows in the vicinity of NGC 2023, but we cannot say with certainty whether it is MIR-63a or b that drives the large southeast-northwest outflow. The CO(2–1) images by Luo et al. (2023) are heavily filtered by the ALMA interferometer and do not give a clear view of the two outflows. We assigned the outflow to MIR-63a because Tobin et al. (2020) found it to be elongated north-south in continuum at 0.87 mm. If the continuum emission traces the accretion disk, it would be roughly orthogonal to the outflow. It is also the more luminous star in the binary system. Nevertheless, it would be very useful to combine the ALMA data with single-dish data in order to better determine the morphology and origin of each outflow in the region in which they are launched.

## 5. Summary and conclusions

The reflection nebula NGC 2023 is illuminated by the Herbig Be star HD 37903. It is the most massive member of a small young cluster with about 30 PMS stars, a few of which are Class I objects and still accrete heavily. We therefore expected that they might power molecular outflows. By analyzing previously published data, we found four molecular outflows. These four outflows are all powered by young stars and are all located in the immediate vicinity of the reflection nebula. All the outflows have roughly similar ages, suggesting that the stars driving them were formed about the same time, which supports the hypothesis that they may have been triggered by the expanding C II region. There are no Class 0 sources in the vicinity of NGC 2023, although young protostars like this exist in the large L 1630 molecular cloud, but they are obviously unrelated to the young NGC 2023 cluster.

*Acknowledgements.* We would like to thank an anonymous referee for the valuable comments and suggestions which helped to improve the manuscript. BM acknowledges the support of the Department of Atomic Energy, Government of India, under Project Identification No. RTI 4002. We also thank Dr. W. Varricattu for advice on how to analyze the UKIDSS images. The paper is based in part on observations made with the NASA/DLR Stratospheric Observatory for Infrared Astronomy (SOFIA). SOFIA is jointly operated by the Universities Space Research Association, Inc. (USRA), under NASA contract NNA17BF53C, and the

Deutsches SOFIA Institut (DSI) under DLR contract 50 OK 0901 to the University of Stuttgart. This work is based in part on data obtained as part of the UKIRT Infrared Deep Sky Survey.

## References

- André, Ph., Men'shchikov, A., Bontemps, S., et al. 2010, *A&A*, 518, L102  
 Bachiller, R., & Pérez Gutiérrez, M. 1997, *ApJ*, 487, L93  
 Bachiller, R., Gómez-González, J. 1992, *A&A Rev.*, 3, 257  
 Bachiller, R., Cernicharo, J., Martín-Pintado, J., et al. 1990, *A&A*, 231, 174  
 Black, J. H., & van Dishoeck, E. F. 1987, *ApJ*, 322, 412  
 Bontemps, S., André, Ph., Könyves, V., et al. 2010, *A&A*, 518, L85  
 Burton, M. G., Geballe, T. R., Brand, P. W. J. L., et al. 1990, *ApJ*, 352, 625  
 Cabrit, S., & Bertout, C. 1992, *A&A*, 261, 274  
 Cabrit, S., Goldsmith, P. F., & Snell, R. L. 1988, *ApJ*, 334, 196  
 Cabrit, S., & Bertout, C. 1986, *ApJ*, 307, 313  
 Casali, M., Adamson, A., Alves de Oliveira, C., et al. 2007, *A&A*, 467, 777  
 Choi, M., Evans II, N. J., & Jaffe, D. T. 1993, *ApJ*, 417, 624  
 Deharveng, L., Schuller, F., Anderson, L. D., et al. 2010, *A&A*, 523, A6  
 DePoy, D. L., Lada, E. A., Gatley, I., et al. 1990 *ApJ*, 356, L55  
 Draine, B. T., & Bertoldi, F. 2000, in *Molecular hydrogen in Space*, Cambridge, UK: Cambridge University Press, Eds. F. Combes & G. Pineau des Forêts, p. 131  
 Draine, B. T., & Bertoldi, F. 1996, *ApJ*, 468, 269  
 Dutta, F., Lee, C.-F., Liu, T., et al. 2020, *ApJS*, 251, 20  
 Elmegreen, B. G., & Lada, C. J. 1977, *ApJ*, 214, 725  
 Fischer, W. J., Megeath, S. T., Furlan, E., et al. 2020, *ApJ*, 905, 119  
 Fleming, B., France, K., Lupu, R. E., & McCandliss, S. R. 2010, *ApJ*, 725, 159  
 Furlan, E., Fischer, W. J., Ali, B., et al. 2016, *ApJS*, 224, 5  
 Güsten, R., Nyman, L.-Å., Schilke, P., et al. 2006, *A&A*, 454, L13  
 Hewett, P. C., Warren, S. J., Leggett, S. K., et al. 2006, *MNRAS*, 367, 454  
 Johnstone, D., Matthews, H., & Mitchell, G. F. 2006, *ApJ*, 639, 259  
 Kauffman, J., Bertoldi, F., Bourke, T. L., et al. 2008, *A&A*, 487, 993  
 Kaufman, M. J., Wolfire, M. G., & Hollenbach, D. J. 2006, *ApJ*, 644, 283  
 Kounkel, M., Covey, K., Moe, M., et al. 2019, *AJ*, 157, 196  
 Kounkel, M., Megeath, S. T., Poteet, C. A., et al. 2016, *ApJ*, 821, 52  
 Könyves, V., André, Ph., Arzoumanian, D., et al. 2020, *A&A*, 635, A34  
 Lada, C. J. 1985, *ARA&A*, 23, 267  
 Lawrence, A., Warren, S. J., Almaini, O., et al. 2007, *MNRAS*, 379, 1599  
 López-García, M. A., López-Santiago, J., Albacete-Colombo, J. F., et al. *MNRAS*, 429, 775  
 Luo, Q.-y., Liu, T., Lee, A. T., et al. 2023, *ApJ*, 952, L2  
 Malin, D. F., Ogura, K., & Walsh, J. R. 1987, *MNRAS*, 227, 361  
 Mangum, J. G., & Shirley, Y. 2015, *PASP*, 127, 266  
 McCartney, M. S. K., Brand, P. W. J. L., Burton, M. G., et al. 1999, *MNRAS*, 307, 315  
 Megeath, S. T., Gutermuth, R., Muzerolle, J., et al. 2012, *AJ*, 144, 192  
 Mookerjee, B., Sandell, G., Güsten, R., et al. 2023, *MNRAS*, 525, 5468  
 Mookerjee, B., Sandell, G., Jarrett, T. H., & McMullin, J. P. 2009, *A&A*, 507, 1485  
 Sandell, G., Mookerjee, M., Güsten, R., et al. 2015, *A&A*, 578, A41  
 Sault, R. J., Teuben, P. J., & Wright, M. C. H. 1995, in *Astronomical Society of the Pacific Conference Series*, Vol. 77, *Astronomical Data Analysis Software and Systems IV*, ed. R. A. Shaw, H. E. Payne, & J. J. E. Hayes, 433–+  
 Scarrott, S. M., Rolph, C. D., & Mannion, M. D. 1989, *MNRAS*, 237, 1027  
 Sellgren, K., Werner, M. W., Ingalls, J. G., et al. 2011, in *EAS Publications Series*, Volume 46, p. 209  
 Sellgren, K. 1984, *ApJ*, 277, 623  
 Sellgren, K. 1983, *AJ*, 88, 1985  
 Sheffer, Y., Wolfire, M. G., Hollenbach, D. J., et al. 2011, *ApJ*, 741, 45  
 Stutz, A. M., Tobin, J. J., Megeath, S. T., et al. 2013, *ApJ*, 767, 36  
 Tobin, J. J., Sheehan, P. D., Megeath, S. T., et al. 2020, *ApJ*, 890, 130  
 Wyrowski, F., Walmsley, C. M., Goss, W. M., et al. 2000, *ApJ*, 543, 245  
 Zavagno, A., Deharveng, L., Comerón, F., et al. 2006, *A&A*, 446, 171

## Appendix A: Position-velocity diagrams

We plot position-velocity diagrams of CO(3–2) and CO(4–3) for the large southeastern outflow from MIR-63, that is, cutting through both the northern and southern red peaks as well as through the outflow from MIR-62.

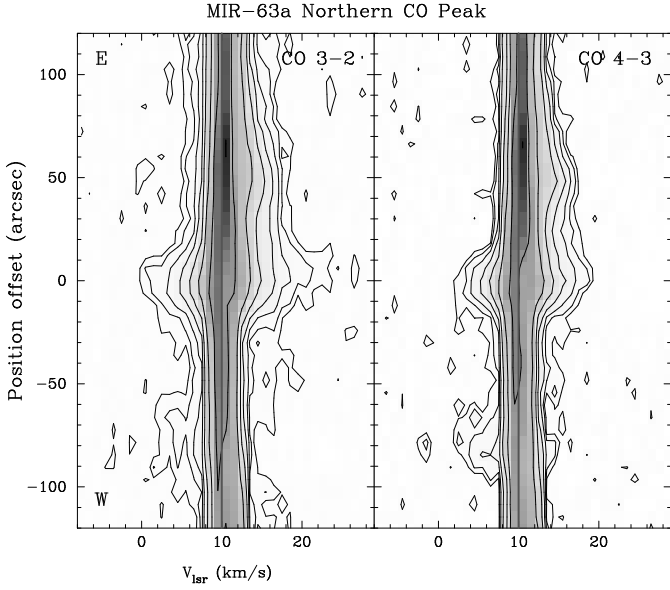


**Fig. A.1.** Position-velocity diagram plotted with contours and overlaid with grayscale through the northern redshifted peak of the large outflow powered by MIR-63a, i.e., at a PA  $\sim 84^\circ$ .

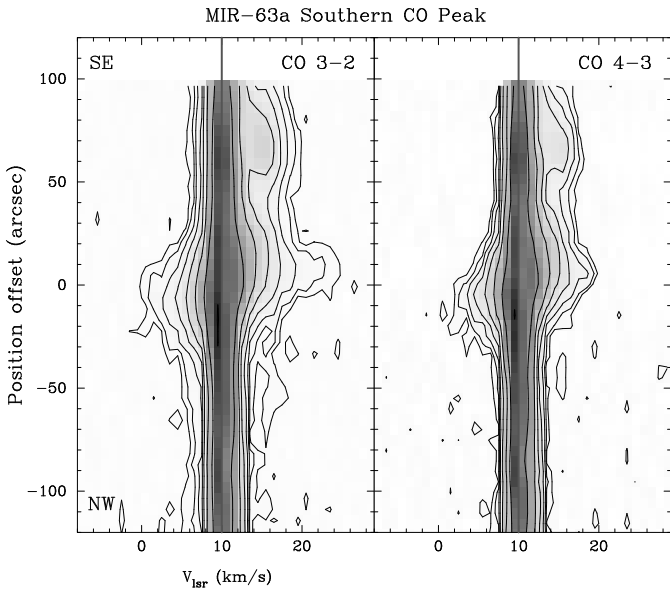


**Fig. A.2.** Position-velocity diagram plotted with contours and overlaid with grayscale through the southern redshifted peak of the large southeastern outflow powered by MIR-63a, i.e., at a PA  $\sim 118^\circ$ ,

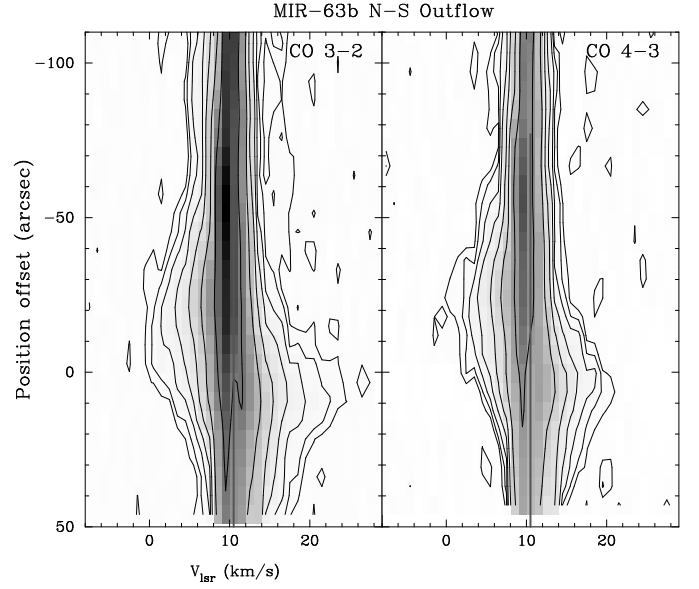


**Fig. A.3.** Position-velocity diagram plotted with contours and overlaid with grayscale of the north-south outflow powered by MIR-63b, i.e., at a PA of  $-10^\circ$ .

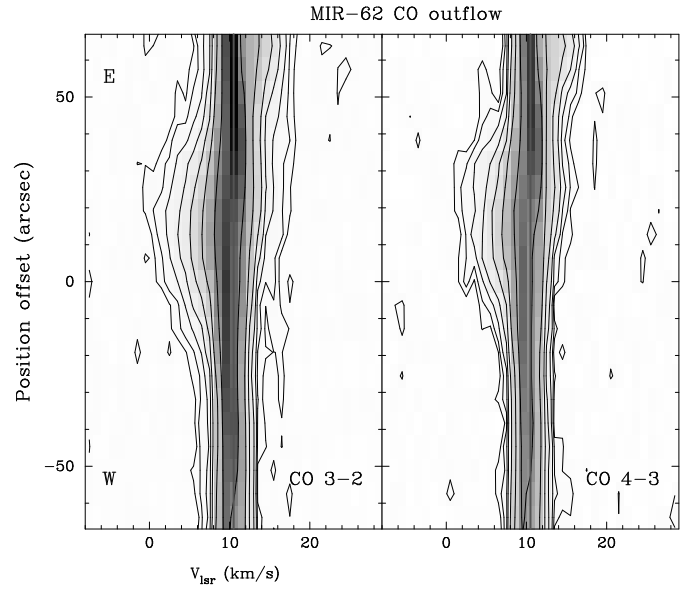


**Fig. A.4.** Position-velocity plot with contours and overlaid with grayscale along the outflow axis of the blueshifted outflow from MIR-62, i.e., at a PA  $\sim 110^\circ$ .